# Hot electron engineering in layered heterojunction for efficient infrared detection

Pushkar Dasika[1], Patrick Hays[2], Suchithra Puliyassery[1], Kenji Watanabe[3], Takashi Taniguchi[4], Seth Ariel Tongay[2] and Kausik Majumdar[1*]

[1]Department of Electrical Communication Engineering, Indian Institute of Science, Bangalore 560012, India

[2]Materials Science and Engineering, School for Engineering of Matter, Transport and Energy, Arizona State University, Tempe, Arizona 85287, USA

[3]Research Center for Electronic and Optical Materials, National Institute for Materials Science, 1-1 Namiki, Tsukuba 305-044, Japan

[4]Research Center for Materials Nanoarchitectonics, National Institute for Materials Science, 1-1 Namiki, Tsukuba 305-044, Japan

Corresponding author*

E-mail: kausikm@iisc.ac.in

**Abstract**

**Although infrared detection is of high technological and strategic importance, the narrow-bandgap materials used for infrared detection often suffer from poor air stability and pose environmental hazards. Hot electron-based detectors avoid such issues by using conventional wide bandgap semiconductors and exploiting intra-band transition. However, hot electron infrared detectors usually suffer from poor quantum efficiency. By photo-exciting $MoS_2$ conduction electrons over a thin barrier layer, here we show that a reversal of the role of the emitter and collector results in a $>$ 1000-fold enhancement in the photoresponse compared with conventional metal/2D semiconductor Schottky diode. We reveal that electron-electron scattering plays a key role in the device performance, which can be effectively tuned by a gate voltage. The photodetector exhibits a nearly flat response up to a measurement wavelength of 1800 nm with a responsivity of 42 mA/W (@1550 nm) at room temperature. We demonstrate an operating frequency of 30 kHz @1550nm excitation (100 kHz @633 nm). The detector chip is integrated with post-processing electronics in a printed circuit board, making it readily usable for system-level applications - a demonstration of heterogeneous integration of 2D materials with conventional electronics.**

**Keywords:** Hot electrons, Infrared Photodetector, van der Waals heterostructure, Broadband, Circuit integration

Infrared (IR) photodetection is of great importance for a wide variety of technologies. Photodetection in the wavelength range of the C band (1528–1561 nm) and the L band (1561–1620 nm) is crucial for low-loss optical communication systems.[1,2] IR photodetectors find extensive applications in imaging,[3] spectroscopy,[4] night vision cameras,[5] and non-invasive biomedical applications.[6] Conventional inter-band photodetectors, where incident photons excite valence band electrons to the conduction band, are limited by their bandgap to detect long wavelength (lower energy) IR radiation. Thus, one must use narrow bandgap semiconductors to detect infrared photons. Unfortunately, these low-bandgap materials usually suffer from problems with stability, complex growth techniques, challenges in integration into standard fabrication flows, and often possess environment-safety-and-health (ESH) related concerns.[7–9]

To this end, two-dimensional layered materials have garnered significant attention in the last decade owing to their extraordinary electrical, mechanical and optical properties.[10–15] Gate-tunability and ease of formation of atomically smooth heterojunctions, with a large library of materials, made them highly attractive for sensitive photodetection applications,[16–20] including the IR regime.[21–28] Unfortunately, there are similar concerns, as stated above, regarding the narrow bandgap layered materials as well.[27–29]

Using widely available, air-stable, large bandgap materials for IR detection alleviates most of the above problems. However, the use of such materials would require a fundamentally different photodetection mechanism. A well-known mechanism is the intraband photo-excitation of carriers and subsequent collection of the hot carriers through a heterojunction,[30,31] also called internal photoemission. Schottky diodes,[30,32–34] and more recently Graphene / 3D semiconductor Schottky junctions[35–38] and metal/2D Semiconductor Schottky junctions[39–43] have been explored for this purpose.

Unfortunately, due to the reasons stated below, for these Schottky junction devices, and more so for those that use 2D layered materials, the achieved internal quantum efficiency is poor, plaguing the achievable photodetection efficiency and hence limiting their widespread

applications. This work aims to propose and demonstrate a different class of intraband IR detector that intrinsically addresses this issue.

**Internal quantum efficiency bottleneck:** A typical Schottky photodiode utilizes the heterojunction between a metal and a bulk semiconductor as shown in Figure 1a. When the metal absorbs photons with energy above the Schottky barrier height (SBH), the hot electrons overcome the barrier and get injected into the semiconductor.[44,45] The built-in electric field in the semiconductor, due to band bending, pulls the photoinduced electrons away from the junction (Figure 1b). The primary bottleneck in the internal quantum efficiency arises from the large free electron density in the metal, which causes rapid carrier relaxation due to ultrafast electron-electron (e-e) scattering (shown by red dashed arrow in Figure 1b) . This results in a small fraction of the generated hot electrons to overcome the Schottky barrier.

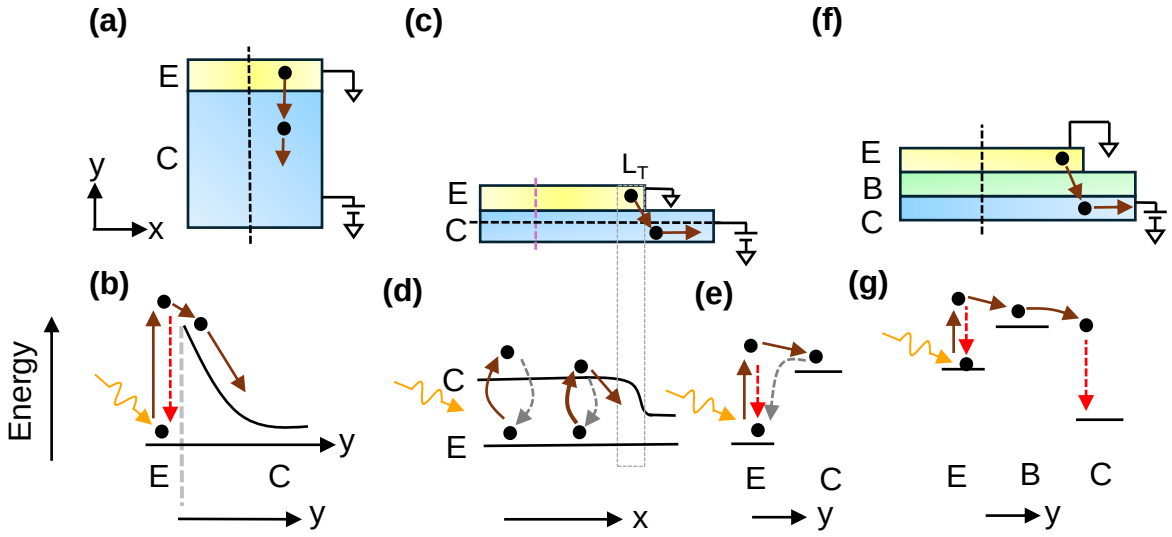


Figure 1: **Internal quantum efficiency in hot electron photodetectors and proposed solution:** (a) A typical Schottky diode-based photodetector with metal emitter (E) and bulk semiconducting collector (C). (b) Band diagram of (a) along the dashed line. (c) A 2D hot-electron photodetector without any barrier layer. (d-e) Band diagrams of (c) along the horizontal black dashed line (d) and along the vertical magenta dashed line (e). The transfer length ($L_T$) region is indicated by the dashed box. (f) The proposed 2D hot-electron photodetector with a barrier layer (shown in green) between the emitter and collector. (g) band diagram of (f) along the dashed line. In each band diagram, the brown solid arrows show the electron path from being excited in the emitter to the collector. The red dashed arrows show carrier relaxation due to e-e scattering. The grey dashed arrows denote the back transfer from the collector to the emitter.

When an ultra-thin layered semiconductor replaces the bulk semiconductor (Figure 1c), and the photocarriers are extracted laterally, there is an additional mechanism that further plagues the quantum efficiency of the photodetector, as explained using the band diagrams in Figure 1d-e. These two band diagrams are plotted along the lateral dashed black line and the vertical dashed magenta line in Figure 1c. Note that the electric field exponentially drops in the lateral direction within a transfer length ($L_T$) from the metal-semiconductor contact edge,[46–49] as marked by the dashed box in Figures 1c-d - degrading the drift of the photo-generated electrons under the metal-semiconductor overlap area. In addition, being the energetically favourable process, in the vertical direction, the photo-induced carriers injected from metal to the layered material are transferred back to the metal at a fast timescale ($\tau_{sm}$) (see Figure 1e). $\tau_{sm}$ is far shorter than the time ($\tau_l$) it takes for the carrier to traverse the lateral metal-semiconductor overlap area. This results in poor carrier injection efficiency unless the photocarrier is generated adjacent to the metal-semiconductor edge.[40,46] This effectively reduces the active area of the photodetector, eventually resulting in a weak photoresponse.

**Proposed device structure:** To circumvent these problems, we propose to use an asymmetric double heterostructure with a thin barrier layer being sandwiched between the emitter (carrier injector) and the collector layers (Figure 1f). Unlike a typical Schottky barrier diode, the collector conduction band (CB) edge is chosen to be energetically lower than the emitter, as shown in Figure 1g. The proposed structure has several important features: (a) The light absorption occurs in a doped semiconductor instead of a metal, and we show later that the interplay between the availability of free electrons and e-e scattering dictates an optimum doping condition that provides the maximum photoresponse. A gate voltage tunes the electrostatic doping in the absorbing layer. (b) The band-offsets of the constituting layers are chosen so that the heterojunction acts as a valve. Once the hot electrons are transferred from the emitter layer to the collector layer and relax to the band edge, the back transfer probability is minimal due to the high energy cost. Note that fast

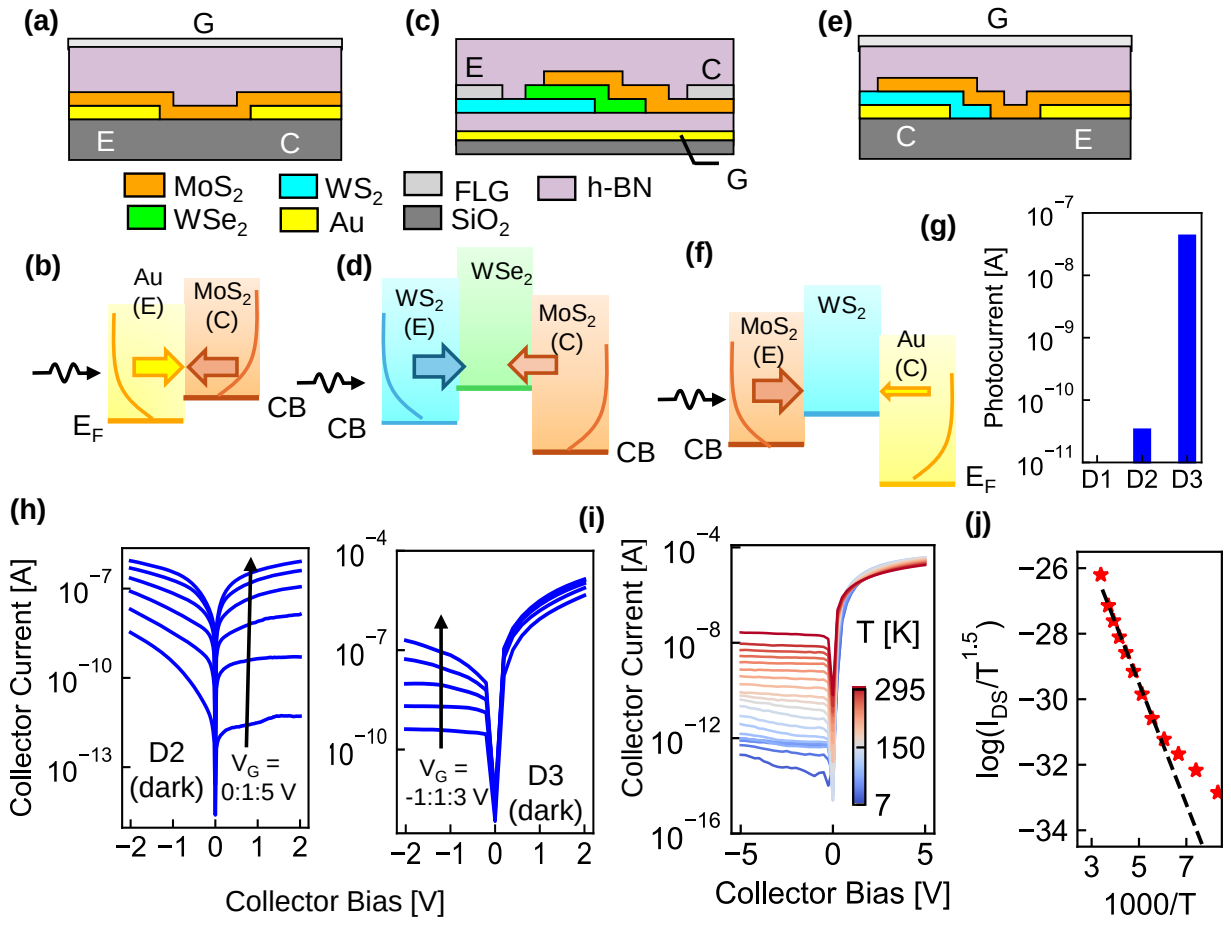


Figure 2: **Proposed structure and relative performance:** (a) Schematic representation of D1, $MoS_2$-Au device without any barrier layer. (b) Band diagram of the conduction band (CB) edge of D1. (c) Schematic of D2, $WS_2/WSe_2/MoS_2$ device where the $WSe_2$ barrier layer is sandwiched between the $WS_2$ emitter and $MoS_2$ collector. The two layers are contacted using a few-layer graphene (FLG). (d) Band diagram of the conduction band edge of D2. (e) Schematic of D3, $MoS_2/WS_2$/Au device with $MoS_2$ emitter and Au collector. (f) Band diagram of the conduction band edge of D3. Gate (G), emitter (E) and collector (C) terminals are indicated in each schematic. The strength of the photoelectron flux in different directions is shown by the width of the corresponding arrows in band diagrams. (g) Comparative photocurrent of the device structures D1, D2 and D3 at similar incident power (1550 nm). (h) Gate bias dependent collector current characteristics of D2 (left panel) and D3 (right panel) as a function of collector bias under dark conditions. (i) Temperature-dependent collector current characteristics of D3 as a function of collector bias under dark conditions. (j) Arrhenius plot to extract Schottky barrier height for Au injection (0.16 eV) for the device D3.

carrier relaxation is detrimental in the emitter but is desirable in the collector as it reduces back transfer probability. Thus, choosing a metal as the collector layer further helps to improve the photoresponse. (c) Note that, in the absence of the barrier layer, the electrons from the emitter will be transferred to the lower-energy collector even under dark condition, and the emitter will not be left with sufficient free electron density for the infrared photo-absorption to take place. The energy barrier provided by the barrier layer blocks such undesirable electron transfer in the dark. (d) The asymmetric band-offsets also help towards the unidirectional flow of photocurrent, improving the overall efficiency (indicated by the thickness of arrows in Figure 2b,d,f). (e) The metal also acts as a back reflector for the incident photons, and the thickness of the entire stack is optimized to improve absorption.

## Results and Discussion

We perform a systematic study by fabricating three different structures (D1, D2, and D3), as schematically depicted in Figures 2a, c and e (SEM images of D2 and D3 are shown in **Supplementary Information S1**). Figures 2b, d and f show the corresponding band diagrams. The thickness of the different layered semiconductors ($MoS_2$, $WS_2$, and $WSe_2$) used is in the range of 5 nm to 15 nm in all the devices (AFM characterization results of devices D2 and D3 are provided in **Supplementary Information S1.**). The details of the fabrication steps are explained in **Methods**. In D1, we directly place $MoS_2$ on Au film, making a conventional Schottky photodiode. D2 consists of a stack of $WS_2$/$WSe_2$/$MoS_2$ layers. The infrared photons excite electrons in the conduction band of the $WS_2$ emitter layer, which are collected by the $MoS_2$ collector through the $WSe_2$ barrier layer. However, the electrons excited in the $MoS_2$ collector layer find it difficult to cross the barrier due to the larger barrier height of $WSe_2$. Finally, in D3, a $WS_2$ barrier layer is sandwiched between Au collector and $MoS_2$ emitter layers. As shown in Figures 2a, c and e, all three structures are controlled by a gate voltage ($V_G$).

Figure 2g shows the relative photoresponse of the three structures when excited with the same optical power ($P_{op}$) of 1550 nm radiation. D1 shows no measurable photocurrent ($I_{ph}$), likely due to strong backscattering, as discussed above (dark current characteristics of D1 are shown in **Supplementary Information S2**). D2 and D3 exhibit appreciable photoresponse; however, $I_{ph}$ from D3 is about 1000-fold stronger than that of D2. The enhanced structural asymmetry and fast relaxation of the injected carriers in the Au collector layer improve the unidirectional flow of $I_{ph}$ in D3 (Figures 2d and f).

To understand the difference in asymmetry between D2 and D3, we perform current-voltage characteristics in the dark condition (Figure 2h-i). The results suggest a more diode-like behaviour in D3 compared with D2, which results from stronger asymmetry. Further, we show the current-voltage characteristics for D3 at different temperatures (Figure 2i). Note that when the electrons are injected from Au to $MoS_2$ (negative collector bias), there is a strong temperature dependence, indicating thermionic emission. We extract an effective SBH of about 0.16 eV from the temperature dependence,[49] as shown in Figure 2j. On the other hand, when electrons are injected from $MoS_2$ to Au (positive collector bias), the temperature dependence is negligible, suggesting that the carriers tunnel through the $WS_2$ barrier layer.

**Engineering the hot electron injection:** When illuminated, the electrons in the conduction band of the emitter layer are excited to higher energy states. These non-equilibrium high energy electrons (hot electrons), in turn, relax initially through e-e scattering in an ultrafast time scale ($\tau_{ee}$) and eventually through phonon scattering at a relatively longer timescale ($\tau_p$).[50–52] However, in the van der Waals junctions under consideration, the hot electrons are also transferred from the emitter to the collector at a fast timescale ($\tau_{ec}$), with $\tau_{ee} < \tau_{ec} < \tau_p$.[53–56] Thus, in our device, the phonon scattering is essentially filtered out, and the injection efficiency to the collector is primarily controlled by the e-e scattering rate, which, in turn, can be controlled by tuning the free electron density in the emitter layer through $V_G$.

We plot the $V_G$ dependence of $I_{ph}$ for both D2 and D3 in the left and right panels of

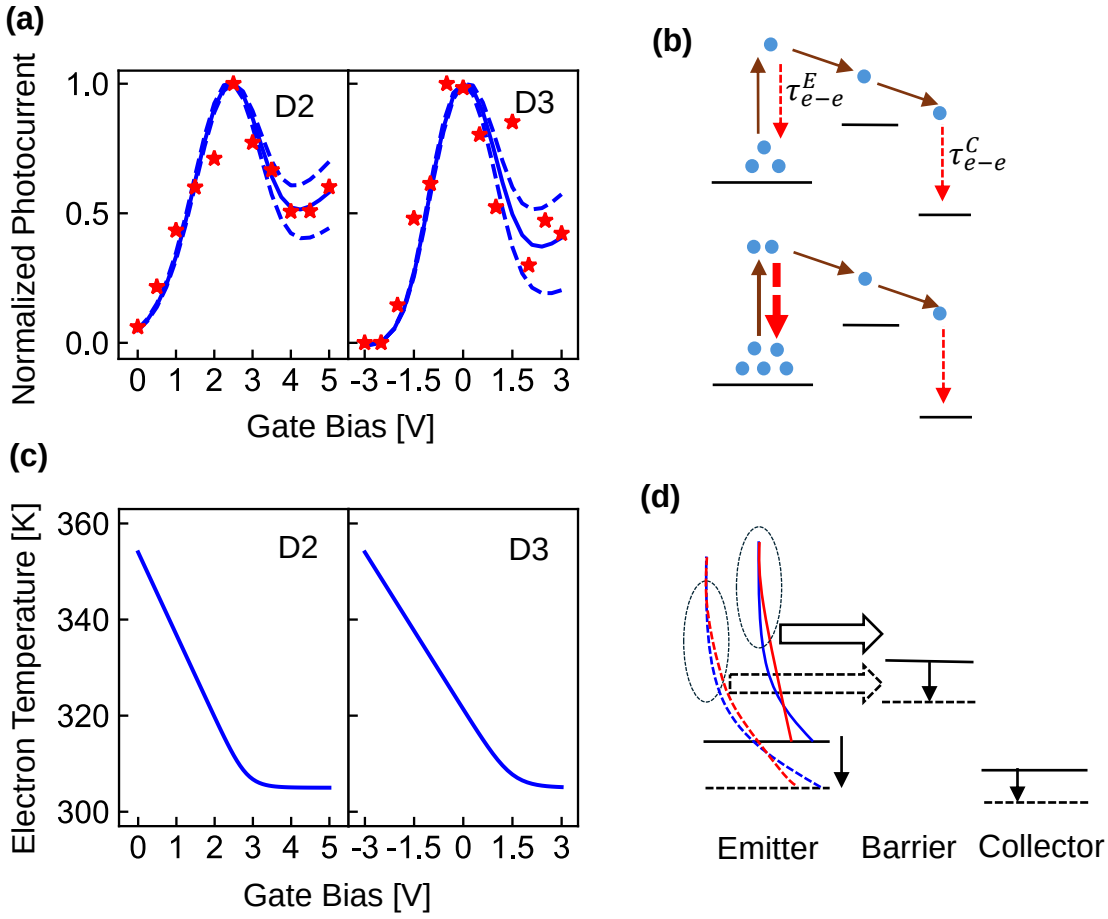


Figure 3: **Tuning photocurrent through controlling e-e scattering:** (a) Photocurrent as a function of gate bias for device structures D2 (left panel) and D3 (right panel). The red stars indicate experimental data, and the blue traces indicate model prediction. The dashed lines show the variation in the fit on changing the simulation parameter (electron temperature) by ±5% (b) Carrier excitation and relaxation for high gate bias (bottom panel, with higher carrier concentration) and low gate bias (top panel, with lower carrier concentration). The relaxation time ($\tau^E_{e-e}$) for higher gate bias is lower. The thickness of different arrows indicates the relative strength of the process. (c) Fitted electron temperature ($T_e$) profile for devices D2 (left panel) and D3 (right panel) as a function of gate bias. (d) Schematic band profiles for two gate biases: low (solid line) and high (dashed line). For each gate bias, the electron distribution is also shown for low $T_e$ and high $T_e$ in blue and red traces, respectively.

Figure 3a, respectively. For both the devices, $I_{ph}$ initially increases with an increase in $V_G$, reaching a maximum value, followed by a reduction in $I_{ph}$ with a further increase in $V_G$. At large $V_G$, we again observe a weak increasing trend of $I_{ph}$ with $V_G$. The initial increase in $I_{ph}$ is expected due to an increase in the available free electron density that can be excited to higher energy states by the incoming infrared radiation (see top panel of Figure 3b). However, when the electron density increases significantly (bottom panel of Figure 3b), the fast relaxation due to enhanced e-e scattering tends to quench the hot electron density, reducing the injection efficiency to the collector, thus degrading the net $I_{ph}$.

We develop a simple physical model to explain such nonmonotonic behaviour quantitatively, as schematically explained in Figure 3d. The details of the model are described in **Supplementary Information S3**. We solve the Poisson equation along the vertical dimension to obtain the electrostatic potential of each layer under dark conditions. We assume that, under illumination, the nonequilibrium electrons available for transfer to the collector can be described by Fermi-Dirac statistics with a higher electron temperature ($T_e$) compared to the lattice temperature ($T_L$). $T_e$ is primarily governed by the e-e scattering under the condition of $\tau_{ee} < \tau_{ec} < \tau_p$. A higher $T_e$ broadens the electron distribution with a longer high energy tail, thus allowing more electrons to cross the barrier layer (Figure 3d). We use $T_e$ as a fitting parameter. The model predicted $I_{ph}$ is shown in solid blue traces in both panels of Figure 3a, and the corresponding fitted $T_e$ is depicted as a function of $V_G$ in Figure 3c.

Consider the case of small $V_G$ in Figure 3d. The conduction band edges are shown in black solid lines, and the corresponding electron distribution with and without photoexcitation is shown in blue and red continuous traces, respectively. Both are calculated, keeping the total electron concentration in the conduction band fixed. This is achieved by calculating a new quasi-Fermi level under illumination. The broader electron distribution under illumination allows more carriers to cross the barrier.

At higher $V_G$, the free electron density increases under dark conditions, and the band edges are energetically shifted downward (shown in black dashed lines). This increment in

the available free electron density results in an enhanced $I_{ph}$ (the rising part in Figure 3a). However, with further increase in $V_G$, $T_e$ also decreases due to faster e-e scattering (Figure 3d), resulting in a narrower electron distribution (dashed traces in blue and red under dark and illumination conditions, respectively), eventually reducing $I_{ph}$. Figure 3c indicates that the fitted $T_e$ gradually reduces with $V_G$ for both D2 and D3, as expected. With an even further increase in $V_G$, the increase in electron concentration slows down significantly due to screening, which in turn flattens out $T_e$ and results in either flattening or slight increment in $I_{ph}$ again. The results suggest an intricate way to tune the quantum efficiency of the photodetector by controlling e-e scattering rate.

**Infrared photodetection performance:** We now focus on device D3 for analyzing the IR detection performance. To understand the steady-state $I_{ph}$ characteristics under 1550 nm excitation, we plot in Figure 4a the device current under laser on (shaded regions) and off conditions at various collector bias ($V_{CE}$) values. The magnitude of the device current systematically increases with $V_{CE}$. The corresponding photocurrent ($I_{ph} = I_{light} - I_{dark}$) is plotted in Figure 4b. Due to an increased bias, a higher electric field helps the electrons excited in the emitter layer to quickly escape to the collector before relaxation, increasing $I_{ph}$. However, due to an increase in $I_{dark}$, larger $V_{CE}$ also increases the shot noise (and thermal noise as well due to substrate heating), as clearly observed in Figure 4b.

The corresponding responsivity ($R = I_{ph}/P_{op}$ at $V_{CE} = 4$ V) is plotted in Figure 4c as a function of incident optical power ($P_{op}$), showing a maximum $R$ of 42 mA/W. Note that, unlike typical 2D material-based photodetectors where $R$ changes by order of magnitude with a variation in $P_{op}$, in our device, $R$ remains a relatively weak function of $P_{op}$. This suggests a negligible role of photocarrier recombination and trapping effects in the device photocurrent.

We extract the noise amplitude ($N$) from the low-frequency temporal response of D3 (Figure 4a) by calculating the standard deviation of the device current under optical illumination. The corresponding signal-to-noise ratio (SNR = $\frac{I_{ph}}{N}$) is plotted in Figure 4d as a

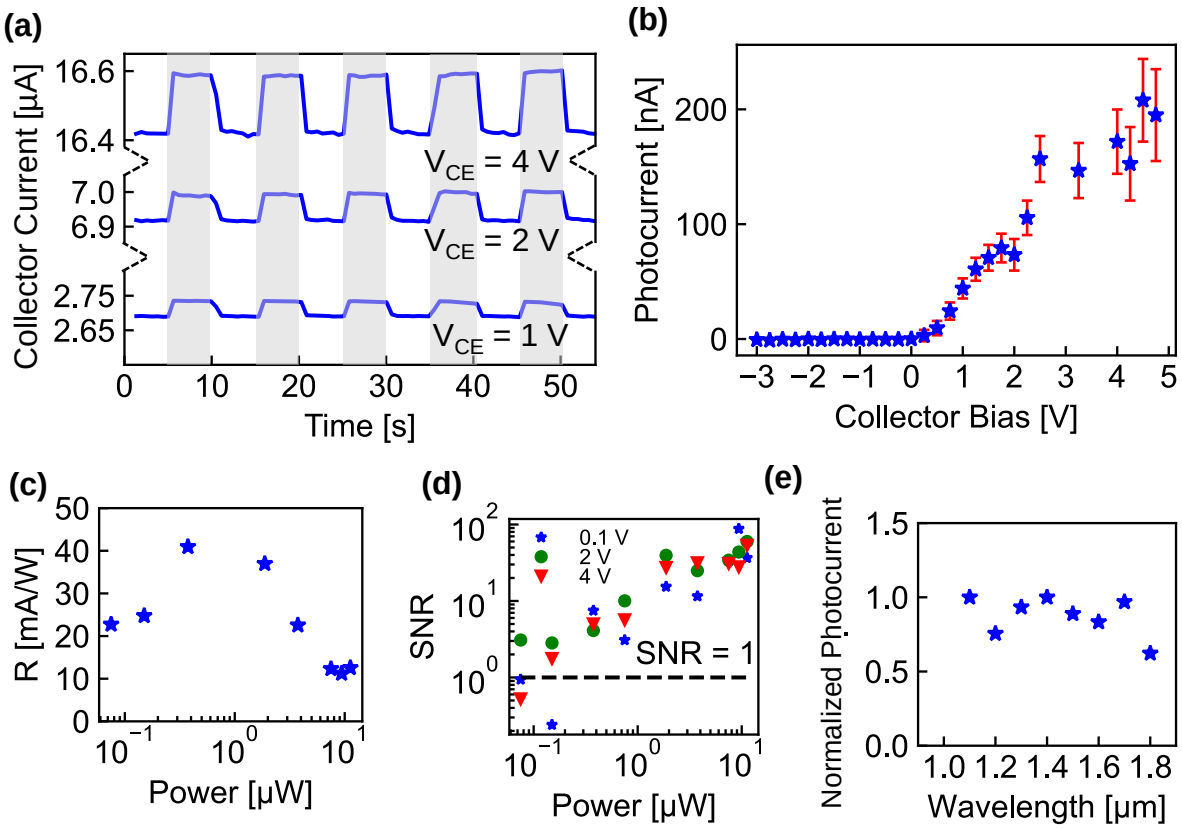


Figure 4: **Infrared detection performance of D3:** (a) Collector current of device D3 with periodic optical (1550 nm) excitation. Grey bands indicate the duration when the optical excitation is on. (b) Collector bias dependence of photocurrent, as extracted from (a). (c) Responsivity (R) of the photodetector as a function of input power at a collector bias of 4 V. (d) The detector's signal-to-noise ratio (SNR) as a function of input power at a collector bias of 4 V (red triangles), 2 V (green dots) and 0.1 V (blue stars). (e) Normalized photocurrent at zero collector bias at various NIR wavelengths.

function of $P_{op}$, for different $V_{CE}$. Interestingly, at low $P_{op}$, we obtain higher SNR at $V_{CE} = 2$ V compared with $V_{CE} = 4$ V due to enhanced shot noise at higher bias. This suggests that an optimal $V_{CE}$ exists for weak signal detection to maximize SNR.

The photoresponse of D3 is nearly flat from 1100 nm to 1800 nm excitation (Figure 4e). A similar broad response is obtained from D2 as well (see **Supplementary Information S4**). This broad response arises because the photon energy at this wavelength range is significantly higher than the band offset between the emitter and the barrier layer. The results from another fabrication run of D3 are shown in **Supplementary Information S5**.

Some more devices with thicker emitter ($MoS_2$) layers are also tested to understand if

thicker emitter layers would help in improved IR absorption. However, we observe that a device with about 50 nm emitter thickness exhibits a poor response (see **Supplementary Information S6**), while another one with about 100 nm emitter layer thickness does not show any discernible photoresponse. This is likely due to a relaxation of the photocarriers before reaching the barrier layer interface and underlines the need for an optimum emitter layer thickness.

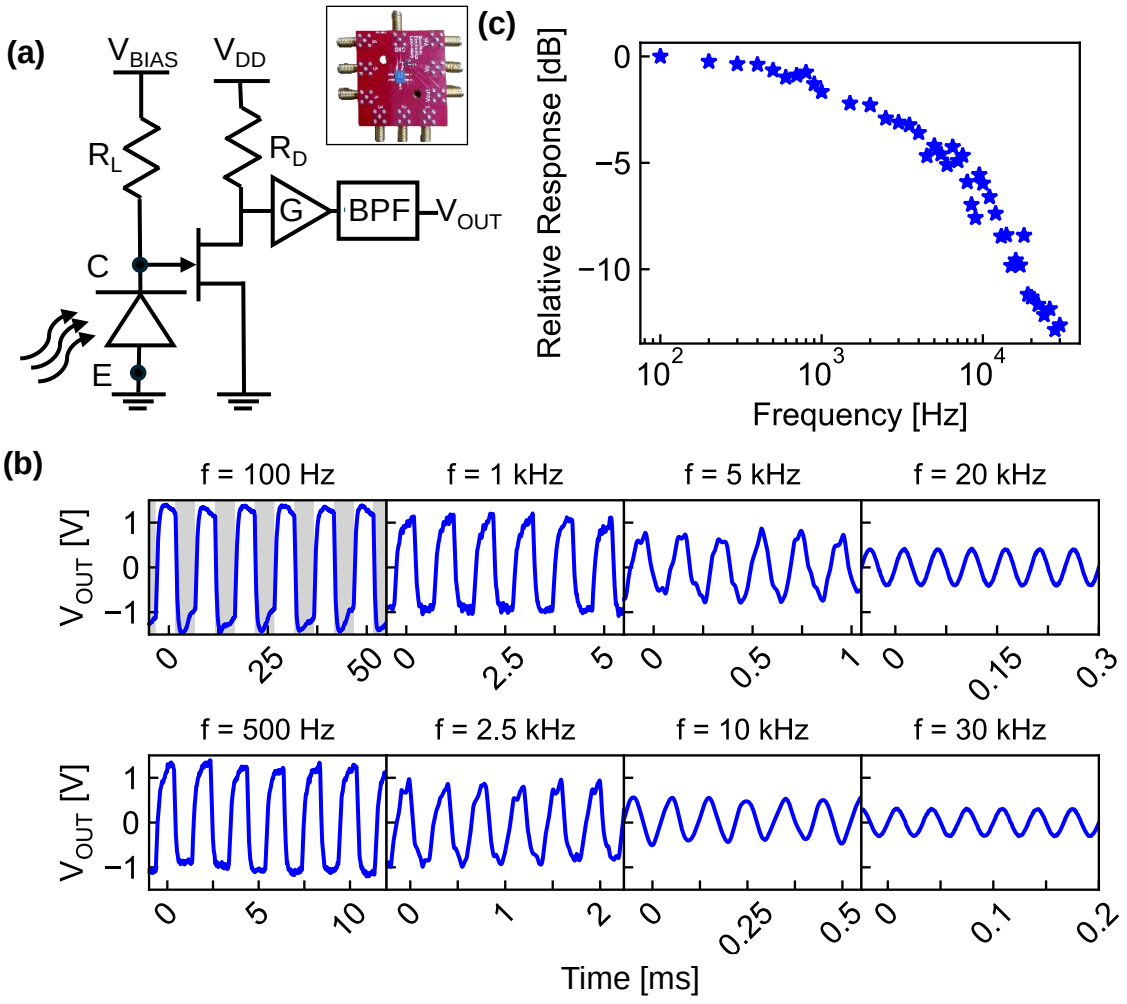


Figure 5: **System integration and speed of operation:** (a) Circuit diagram representing the setup to measure the frequency response. Inset: The 2D photodetector chip (in blue colour at the centre) integrated into a PCB with other off-chip electronics. (b) Temporal response of the detector D3 from 100 Hz to 30 kHz. Signal above the noise floor can be observed up to 30 kHz. (c) Relative response $[V_{OUT}(f)/V_{OUT}(100\ Hz)]$ of the device D3 in dB as a function of laser modulation frequency.

Next, we measure the frequency response of D3 using a setup shown in Figure 5a. The

detector is connected to a $V_{BIAS} = -4$ V through an external load resistor ($R_L$) of 570 $k\Omega$, which helps convert the output current to a voltage signal. The signal from the photodetector is fed to a JFET-based single-stage amplifier with a load resistance ($R_D$) of 100 $\Omega$. The JFET is biased with a $V_{DD} = 3$ V. The detector, external resistors and the JFET are integrated into a printed circuit board (PCB) (inset of Figure 5a). The signal output is then further bandpass-filtered with an input gain of 20 dB and observed in an oscilloscope.

The photodetector is illuminated with a 1550 nm laser at varying frequencies. The temporal response of the output signal for different laser modulation frequencies is shown in Figure 5b. The time during which light is illuminated is shown in grey bands in the top left panel. A signal above the noise floor could be observed up to $\sim$30 KHz. Figure 5c shows relative photoresponse (in dB) as a function of the laser intensity modulation frequency.

The measured frequency response is primarily limited by the gain-bandwidth product of the external measurement setup and not by the intrinsic device. The limiting factor arises from the relatively large input capacitance of the JFET. The intrinsic response from the device itself could be much faster, as all the physical processes involved in the detection mechanism are fast. In **Supplementary Information S7**, we show the device's response to 633 nm excitation (which allows bandgap absorption and hence a stronger signal), demonstrating a detectable response above the noise floor up to 100 KHz. A table benchmarking our device performance with other works is given in **Supplementary Information S8**.

# Conclusion

To conclude, we demonstrate efficient broadband infrared response using a different class of intra-band photodetector where the internal quantum efficiency is intrinsically improved through elegant hot electron management. The simplicity of the design makes the device readily integrable with different photo-excitation schemes, such as with a waveguide. We also demonstrate the heterogeneous integration of the photodetector chip with post-processing

electronics on a printed circuit board, making it immediately usable at a system level.

# Methods

**Device fabrication and characterization:** First, contacts are defined by optical lithography on a 285 nm thermally grown $SiO_2$ coated Si substrate. This is followed by Ti (20 nm) and Au (40 nm) deposition by DC sputtering and lift-off. Then, layers of each material of appropriate thickness for the respective devices are exfoliated on a PDMS stamp and transferred sequentially on the pre-patterned substrate. Finally, the devices are annealed at 150°C in a vacuum ($10^{-6}$ Torr) for three hours to form good contacts.

DC electrical and optical characterization of the devices is performed under vacuum ($10^{-4}$ Torr) in Lakeshore CRX-6.5K probe station equipped with an optical fibre probe. For frequency response measurement, the substrate with the device is wire-bonded on a PCB. The PCB also contains an n-channel MMBFU310LT1G JFET from Onsemi and surface mount resistors of appropriate value. The output of the PCB is connected to a digital storage oscilloscope through a gain stage and a bandpass filter.

The photocurrent of the device has been measured by shining light on the device using a fibre of 100 $\mu$m diameter. The device is kept at a distance of about 50 $\mu$m from the device at an oblique angle of about 30°. The power of the light coming out is measured using a power meter. Since the spot size ($A_{fiber}$) from the fibre is much larger than the device area ($A_{device}$), the responsivity is calculated as

$$R = \frac{P_{op}}{I_{Ph}} \frac{A_{fiber}}{A_{device}} \tag{1}$$

# Acknowledgements

K.M. acknowledges useful discussion with Andrew Lord. K.M. acknowledges the support from a grant under SERB TETRA, grants from Indian Space Research Organization (ISRO),

a grant from British Telecom India Research Centre (BTIRC), a grant from I-HUB QTF, IISER Pune, and a seed funding under Quantum Research Park (QuRP) from Karnataka Innovation and Technology Society (KITS), K-Tech, Government of Karnataka. K.W. and T.T. acknowledge support from the JSPS KAKENHI (Grant Numbers 21H05233 and 23H02052) and World Premier International Research Center Initiative (WPI), MEXT, Japan. S.T. acknowledges primary support from DOE-SC0020653 (materials synthesis), Applied Materials Inc., NSF CMMI 1825594 (NMR and TEM studies), NSF DMR-1955889 (magnetic measurements), NSF CBET 2206987, DMR 2111812, and CMMI 2129412, and support from Lawrence Semiconductors.

# Competing Interests

The authors declare no competing financial or non-financial interests.

# Associated Content

### Data Availability Statement

The data supporting this study's findings are available from the corresponding author upon request.

### Supporting Information

The Supporting Information is available free of charge at XXX. SEM and AFM data of devices D2 and D3, electrical characteristics of device D1 under dark conditions, hot-electron induced photocurrent model, the response of structure D2 to various wavelengths, characterization of additional D3 device, $MoS_2$ thickness-dependent photoresponse of D3, the frequency response of D3 for excitation with 633 nm radiation and performance benchmarking.

# References


(1) Kaushal, H.; Kaddoum, G. Optical Communication in Space: Challenges and Mitigation Techniques. *IEEE Communications Surveys & Tutorials* **2017**, *19*, 57–96.

(2) Hui, R. *Introduction to Fiber-Optic Communications*; Academic Press, 2019.

(3) Lee, S. J.; Ku, Z.; Barve, A.; Montoya, J.; Jang, W.-Y.; Brueck, S.; Sundaram, M.; Reisinger, A.; Krishna, S.; Noh, S. K. A monolithically integrated plasmonic infrared quantum dot camera. *Nature Communications* **2011**, *2*, 286.

(4) Yeh, K.; Sharma, I.; Falahkheirkhah, K.; Confer, M. P.; Orr, A. C.; Liu, Y.-T.; Phal, Y.; Ho, R.-J.; Mehta, M.; Bhargava, A.; others Infrared spectroscopic laser scanning confocal microscopy for whole-slide chemical imaging. *Nature Communications* **2023**, *14*, 5215.

(5) Wang, F.; Hu, F.; Dai, M.; Zhu, S.; Sun, F.; Duan, R.; Wang, C.; Han, J.; Deng, W.; Chen, W.; others A two-dimensional mid-infrared optoelectronic retina enabling simultaneous perception and encoding. *Nature Communications* **2023**, *14*, 1938.

(6) Hutchinson, L. Digital infrared breast scan shows promise for detecting cancer. *Nature Reviews Clinical Oncology* **2010**, *7*, 483–483.

(7) Levine, B. Quantum-well infrared photodetectors. *Journal of Applied Physics* **1993**, *74*, R1–R81.

(8) Phillips, J. Evaluation of the fundamental properties of quantum dot infrared detectors. *Journal of Applied Physics* **2002**, *91*, 4590–4594.

(9) Guyot-Sionnest, P.; Ackerman, M. M.; Tang, X. Colloidal quantum dots for infrared detection beyond silicon. *The Journal of Chemical Physics* **2019**, *151*.

(10) Fiori, G.; Bonaccorso, F.; Iannaccone, G.; Palacios, T.; Neumaier, D.; Seabaugh, A.; Banerjee, S. K.; Colombo, L. Electronics based on two-dimensional materials. *Nature Nanotechnology* **2014**, *9*, 768–779.

(11) Chhowalla, M.; Jena, D.; Zhang, H. Two-dimensional semiconductors for transistors. *Nature Reviews Materials* **2016**, *1*, 1–15.

(12) Lin, Z.; Huang, Y.; Duan, X. Van der Waals thin-film electronics. *Nature Electronics* **2019**, *2*, 378–388.

(13) Mak, K. F.; Shan, J. Photonics and optoelectronics of 2D semiconductor transition metal dichalcogenides. *Nature Photonics* **2016**, *10*, 216–226.

(14) An, J.; Zhao, X.; Zhang, Y.; Liu, M.; Yuan, J.; Sun, X.; Zhang, Z.; Wang, B.; Li, S.; Li, D. Perspectives of 2D materials for optoelectronic integration. *Advanced Functional Materials* **2022**, *32*, 2110119.

(15) Akinwande, D.; Petrone, N.; Hone, J. Two-dimensional flexible nanoelectronics. *Nature Communications* **2014**, *5*, 5678.

(16) Murali, K.; Abraham, N.; Das, S.; Kallatt, S.; Majumdar, K. Highly sensitive, fast graphene photodetector with responsivity $> 10^6$ A/W using a floating quantum well gate. *ACS applied materials & interfaces* **2019**, *11*, 30010–30018.

(17) Nur, R.; Tsuchiya, T.; Toprasertpong, K.; Terabe, K.; Takagi, S.; Takenaka, M. High responsivity in MoS2 phototransistors based on charge trapping $HfO_2$ dielectrics. *Communications Materials* **2020**, *1*, 103.

(18) Gardella, M.; Zambito, G.; Ferrando, G.; Bisio, F.; Giordano, M. C.; de Mongeot, F. B. Large area van der Waals $MoS_2 - WS_2$ heterostructures for visible-light energy conversion. *RSC Applied Interfaces* **2024**,

(19) Xue, Y.; Zhang, Y.; Liu, Y.; Liu, H.; Song, J.; Sophia, J.; Liu, J.; Xu, Z.; Xu, Q.; Wang, Z.; others Scalable production of a few-layer $MoS_2/WS_2$ vertical heterojunction array and its application for photodetectors. *ACS Nano* **2016**, *10*, 573–580.

(20) Lin, X.; Wang, F.; Shan, X.; Miao, Y.; Chen, X.; Yan, M.; Zhang, L.; Liu, K.; Luo, J.; Zhang, K. High-performance photodetector and its optoelectronic mechanism of $MoS_2/WS_2$ vertical heterostructure. *Applied Surface Science* **2021**, *546*, 149074.

(21) Guo, Q.; Pospischil, A.; Bhuiyan, M.; Jiang, H.; Tian, H.; Farmer, D.; Deng, B.; Li, C.; Han, S.-J.; Wang, H.; others Black phosphorus mid-infrared photodetectors with high gain. *Nano Letters* **2016**, *16*, 4648–4655.

(22) Wu, D.; Wang, Y.; Zeng, L.; Jia, C.; Wu, E.; Xu, T.; Shi, Z.; Tian, Y.; Li, X.; Tsang, Y. H. Design of 2D layered $PtSe_2$ heterojunction for the high-performance, room-temperature, broadband, infrared photodetector. *ACS Photonics* **2018**, *5*, 3820–3827.

(23) Amani, M.; Tan, C.; Zhang, G.; Zhao, C.; Bullock, J.; Song, X.; Kim, H.; Shrestha, V. R.; Gao, Y.; Crozier, K. B.; others Solution-synthesized high-mobility tellurium nanoflakes for short-wave infrared photodetectors. *ACS Nano* **2018**, *12*, 7253–7263.

(24) Huang, L.; Dong, B.; Guo, X.; Chang, Y.; Chen, N.; Huang, X.; Liao, W.; Zhu, C.; Wang, H.; Lee, C.; others Waveguide-integrated black phosphorus photodetector for mid-infrared applications. *ACS Nano* **2018**, *13*, 913–921.

(25) Mueller, T.; Xia, F.; Avouris, P. Graphene photodetectors for high-speed optical communications. *Nature Photonics* **2010**, *4*, 297–301.

(26) Kawano, Y. Wide-band frequency-tunable terahertz and infrared detection with graphene. *Nanotechnology* **2013**, *24*, 214004.

(27) Abraham, N.; Watanabe, K.; Taniguchi, T.; Majumdar, K. Room Temperature Single Photon Detection at 1550 nm Using van der Waals Heterojunction. *Advanced Functional Materials* **2024**, *n/a*, 2406510.

(28) Wang, F.; Zhu, S.; Chen, W.; Han, J.; Duan, R.; Wang, C.; Dai, M.; Sun, F.; Jin, Y.; Wang, Q. J. Multidimensional detection enabled by twisted black arsenic–phosphorus homojunctions. *Nature Nanotechnology* **2024**, *19*, 455–462.

(29) Chen, X.; Lu, X.; Deng, B.; Sinai, O.; Shao, Y.; Li, C.; Yuan, S.; Tran, V.; Watanabe, K.; Taniguchi, T.; others Widely tunable black phosphorus mid-infrared photodetector. *Nature Communications* **2017**, *8*, 1672.

(30) Peters, D. An infrared detector utilizing internal photoemission. *Proceedings of the IEEE* **1967**, *55*, 704–705.

(31) Sze, S. M. *Semiconductor devices: physics and technology*; John wiley & sons, 2008.

(32) Elabd, H.; Villani, T.; Kosonocky, W. Palladium-silicide Schottky-barrier IR-CCD for SWIR applications at intermediate temperatures. *IEEE Electron Device Letters* **1982**, *3*, 89–90.

(33) Kosonocky, W.; Shallcross, F.; Villani, T.; Groppe, J. 160 × 244 Element PtSi Schottky-barrier IR-CCD image sensor. *IEEE Transactions on Electron Devices* **1985**, *32*, 1564–1573.

(34) Chen, C.; Nechay, B.; Tsaur, B.-Y. Ultraviolet, visible, and infrared response of PtSi Schottky-barrier detectors operated in the front-illuminated mode. *IEEE Transactions on Electron Devices* **1991**, *38*, 1094–1103.

(35) Zeng, L.-H.; Wang, M.-Z.; Hu, H.; Nie, B.; Yu, Y.-Q.; Wu, C.-Y.; Wang, L.; Hu, J.-G.; Xie, C.; Liang, F.-X.; others Monolayer graphene/germanium Schottky junction

as high-performance self-driven infrared light photodetector. *ACS Applied Materials & Interfaces* **2013**, *5*, 9362–9366.

(36) Casalino, M.; Sassi, U.; Goykhman, I.; Eiden, A.; Lidorikis, E.; Milana, S.; De Fazio, D.; Tomarchio, F.; Iodice, M.; Coppola, G.; others Vertically illuminated, resonant cavity enhanced, graphene–silicon Schottky photodetectors. *ACS Nano* **2017**, *11*, 10955–10963.

(37) Goykhman, I.; Sassi, U.; Desiatov, B.; Mazurski, N.; Milana, S.; De Fazio, D.; Eiden, A.; Khurgin, J.; Shappir, J.; Levy, U.; others On-chip integrated, silicon–graphene plasmonic Schottky photodetector with high responsivity and avalanche photogain. *Nano Letters* **2016**, *16*, 3005–3013.

(38) Amirmazlaghani, M.; Raissi, F.; Habibpour, O.; Vukusic, J.; Stake, J. Graphene-Si Schottky IR Detector. *IEEE Journal of Quantum Electronics* **2013**, *49*, 589–594.

(39) Hong, T.; Chamlagain, B.; Hu, S.; Weiss, S. M.; Zhou, Z.; Xu, Y.-Q. Plasmonic hot electron induced photocurrent response at $MoS_2$–metal junctions. *ACS Nano* **2015**, *9*, 5357–5363.

(40) Hong, C.; Oh, S.; Dat, V. K.; Pak, S.; Cha, S.; Ko, K.-H.; Choi, G.-M.; Low, T.; Oh, S.-H.; Kim, J.-H. Engineering electrode interfaces for telecom-band photodetection in $MoS_2$/Au heterostructures via sub-band light absorption. *Light: Science & Applications* **2023**, *12*, 280.

(41) Zhang, Q.; Ji, Y.; Hu, S.; Li, Z.; Li, C.; Gu, L.; Tian, R.; Zhang, J.; Fang, L.; Zhao, B.; others High-responsivity $MoS_2$ hot-electron telecom-band photodetector integrated with microring resonator. *Applied Physics Letters* **2022**, *120*.

(42) Li, Z.; Hu, S.; Zhang, Q.; Tian, R.; Gu, L.; Zhu, Y.; Yuan, Q.; Yi, R.; Li, C.; Liu, Y.; others Telecom-band waveguide-integrated $MoS_2$ photodetector assisted by hot electrons. *ACS Photonics* **2022**, *9*, 282–289.

(43) Hong, C.; Jang, S. G.; Yu, Y.-J.; Kim, J.-H. Hot electron dynamics in $MoS_2$/Pt van der Waals electrode interface for self-powered hot electron photodetection. *Advanced Materials Interfaces* **2023**, *10*, 2300140.

(44) Mooney, J.; Silverman, J. The theory of hot-electron photoemission in Schottky-barrier IR detectors. *IEEE Transactions on Electron Devices* **1985**, *32*, 33–39.

(45) Scales, C.; Berini, P. Thin-Film Schottky Barrier Photodetector Models. *IEEE Journal of Quantum Electronics* **2010**, *46*, 633–643.

(46) Somvanshi, D.; Kallatt, S.; Venkatesh, C.; Nair, S.; Gupta, G.; Anthony, J. K.; Karmakar, D.; Majumdar, K. Nature of carrier injection in metal/2D-semiconductor interface and its implications for the limits of contact resistance. *Physical Review B* **2017**, *96*, 205423.

(47) Xia, F.; Perebeinos, V.; Lin, Y.-m.; Wu, Y.; Avouris, P. The origins and limits of metal–graphene junction resistance. *Nature Nanotechnology* **2011**, *6*, 179–184.

(48) Szabó, Á.; Jain, A.; Parzefall, M.; Novotny, L.; Luisier, M. Electron transport through metal/MoS2 interfaces: edge-or area-dependent process? *Nano letters* **2019**, *19*, 3641–3647.

(49) Murali, K.; Dandu, M.; Watanabe, K.; Taniguchi, T.; Majumdar, K. Accurate Extraction of Schottky Barrier Height and Universality of Fermi Level De-Pinning of van der Waals Contacts. *Advanced Functional Materials* **2021**, *31*, 2010513.

(50) Mylnikov, D. A.; Kashchenko, M. A.; Kapralov, K. N.; Ghazaryan, D. A.; Vdovin, E. E.; Morozov, S. V.; Novoselov, K. S.; Bandurin, D. A.; Chernov, A. I.; Svintsov, D. A. Infrared photodetection in graphene-based heterostructures: bolometric and thermoelectric effects at the tunneling barrier. *npj 2D Materials and Applications* **2024**, *8*, 34.

(51) Wittenbecher, L.; Vinas Bostrom, E.; Vogelsang, J.; Lehman, S.; Dick, K. A.; Verdozzi, C.; Zigmantas, D.; Mikkelsen, A. Unraveling the ultrafast hot electron dynamics in semiconductor nanowires. *ACS nano* **2021**, *15*, 1133–1144.

(52) Chen, I.-J.; Limpert, S.; Metaferia, W.; Thelander, C.; Samuelson, L.; Capasso, F.; Burke, A. M.; Linke, H. Hot-carrier extraction in nanowire-nanoantenna photovoltaic devices. *Nano Letters* **2020**, *20*, 4064–4072.

(53) Hong, X.; Kim, J.; Shi, S.-F.; Zhang, Y.; Jin, C.; Sun, Y.; Tongay, S.; Wu, J.; Zhang, Y.; Wang, F. Ultrafast charge transfer in atomically thin $MoS_2$/$WS_2$ heterostructures. *Nature Nanotechnology* **2014**, *9*, 682–686.

(54) Trovatello, C.; Piccinini, G.; Forti, S.; Fabbri, F.; Rossi, A.; De Silvestri, S.; Coletti, C.; Cerullo, G.; Dal Conte, S. Ultrafast hot carrier transfer in $WS_2$/graphene large area heterostructures. *npj 2D Materials and Applications* **2022**, *6*, 24.

(55) Zhou, H.; Chen, Y.; Zhu, H. Harnessing Hot Carriers in Two-Dimensional Materials. *The Journal of Physical Chemistry C* **2024**,

(56) Sun, C.; Zhou, H.; Sheng, T.; Li, S.; Zhu, H. Ultrafast interlayer charge transfer outcompeting intralayer valley relaxation in few-layer 2D heterostructures. *ACS Nano* **2023**, *18*, 931–938.